JOURNAL OF THEORETICAL
AND APPLIED MECHANICS
https://doi.org/10.15632/jtam-pl/241697
ONLINE FIRST

WHEEL TREAD WEAR ANALYSIS OF HEAVY-HAUL WAGONS ON LONG DOWNHILL LINES CONSIDERING CYCLIC BRAKING AND TEMPERATURE RISE

Yong LI, Wangcai DING*

School of Mechanical Engineering, Lanzhou Jiaotong University, Lanzhou, China
*corresponding author, *dingwc@mail.lzjtu.cn*

Frequent cyclic braking on long downhill routes changes wheel–rail creepage and heats the wheel tread. This study evaluates the resulting wheel–rail wear of a heavy-haul wagon using a sequential calculation framework. Braking and coupler-force histories from train longitudinal dynamics are transferred to a three-dimensional vehicle multibody model. The resulting contact quantities drive a reduced-order layered wheel–block thermal calculation and a temperature-dependent Archard wear calculation. The framework represents the actual line profile, frictional heat inputs at the wheel–block and wheel–rail interfaces, and temperature-dependent contact and wear parameters. For a 52 km section of the Datong–Qinhuangdao Railway, the predicted representative wheel-tread temperature reaches 339.8 °C. The circumferentially averaged wear depth varies across the tread after one run. Route-grouped comparisons show higher mean wear rates during braking, at elevated temperatures, and on curves; the curved-to-straight-track ratio is the largest of the reported comparisons. These findings provide a basis for evaluating braking strategies and identifying wheel-tread regions requiring closer inspection in heavy-haul operations on long downhill lines.

Keywords: heavy-haul wagon; wheel tread wear; cyclic braking; multibody dynamics.



Articles in JTAM are published under Creative Commons Attribution 4.0 International.
Unported License https://creativecommons.org/licenses/by/4.0/deed.en.
By submitting an article for publication, the authors consent to the grant of the said license.

1. Introduction

Heavy-haul railways provide an important means of transporting bulk freight in China because they combine large carrying capacity with high operating efficiency and relatively low cost. Cyclic braking is normally used to regulate train speed on extended downhill sections. This operating mode increases wheel–rail creepage and heats the wheel tread, making the tread more vulnerable to damage. As summarized by Akama (2025), wear and rolling contact fatigue (RCF) are the principal tread-damage mechanisms, and their competition generally determines the final surface condition.

Current wheel tread wear prediction methods mainly follow two routes: data-driven prediction and multibody-dynamics-simulation (MBS)-based calculation. Data-driven studies use intelligent algorithms to relate tread wear to operating variables such as axle load, vehicle speed, and track geometry (Liu *et al.*, 2025). Such models enable rapid evaluation, but their reliability depends strongly on the coverage and representativeness of the training samples, so extrapolation beyond the database is limited. In an MBS-based procedure, vehicle dynamic responses are calculated first, followed by determination of wheel–rail forces and contact conditions; an appropriate wear law is then applied. Although this route requires more computation, it provides direct insight into contact mechanics, wear development, and the governing operating factors, and is therefore widely used in mechanism-based studies. Ye *et al.* (2023) combined Hertz contact and FASTSIM with the Archard equation to predict tread wear. Wen *et al.* (2025) used the Kik–Piotrowski and FASTRIP methods for non-Hertzian contact and included the influence

of wheel temperature in locomotive-wheel wear calculations. Miao *et al.* (2024) employed the USFD model and incorporated elastic deformation of both contacting bodies.

Vehicle motion governs wheel–rail loading and creepage and thereby affects tread wear. A number of earlier studies evaluated wheel damage with simplified vehicle dynamics or prescribed contact states (Magelli & Zampieri, 2024; Liu *et al.*, 2026). Such treatments do not fully reproduce the longitudinal loads acting at the two ends of a wagon and may therefore differ from the contact conditions experienced in service. The sensitivity of wheel–rail contact to the overall vehicle response has been demonstrated in previous work (Wu *et al.*, 2024; Zhang *et al.*, 2023), indicating that three-dimensional MBS models are preferable for wear and RCF assessment. Chen *et al.* (2026) examined braking-related wheel damage while incorporating train longitudinal dynamics and coupler forces. Accordingly, the train-level longitudinal response should be solved before the corresponding external loads and motion histories are introduced into the vehicle model (Doan Van *et al.*, 2026; Zou *et al.*, 2026). Combining the two levels of dynamics improves the representation of the operating contact state used for wheel-wear calculation.

Tread braking converts friction work at the brake block–wheel interface into heat and raises the wheel-surface temperature. Temperature-dependent changes in elastic modulus, hardness, and interfacial friction may alter contact conditions and material removal; the friction response depends on the contacting materials and operating conditions. Using a full-scale tread-braking rig, Handa *et al.* (2020) quantified the effect of tread temperature on wheel wear and proposed a temperature-dependent wear-rate relation. Chen *et al.* (2017) studied the influence of braking-induced temperature rise on heavy-haul wheel wear under emergency braking. Wang *et al.* (2024) further evaluated temperature effects on wheel RCF during braking and quantified the roles of the track profile, running speed, and wheel temperature in RCF life.

Despite progress in wheel-wear prediction, the joint influence of the train longitudinal response, cyclic tread braking, wheel heating, and actual line curvature remains insufficiently resolved for heavy-haul wagons on long downhill routes. The present study therefore links train longitudinal dynamics, a three-dimensional vehicle multibody model, a reduced-order wheel–block thermal model, and a temperature-dependent Archard wear model. The coupling is sequential: mechanical outputs provide thermal inputs, and calculated wheel temperature modifies the subsequent contact and wear calculation. The objective is to examine wheel–rail wear during a single downhill run, rather than to resolve local three-dimensional temperature fields, thermoelastic stresses, or brake-block wear. The main contribution is an integrated assessment of wheel–rail wear that accounts for train-level braking and coupler loads together with temperature-dependent contact and wear properties under actual downhill route conditions. The analysis identifies lateral tread regions and operating conditions associated with increased predicted wear, providing a basis for subsequent evaluation of braking strategies and targeted wheel-tread inspection on long downhill lines.

2. Methodology

The analysed system comprises a C80 wagon, its tread brakes, and the wheel–rail contacts. The calculation links four stages: train longitudinal dynamics, vehicle multibody dynamics in SIMPACK, a layered wheel–block thermal calculation, and temperature-dependent wheel–rail wear post-processing. Train-level loads drive the vehicle model, whose contact outputs determine the frictional heat inputs and wear-loading history. The calculated wheel temperature is used to update contact dimensions and wear parameters in post-processing. This is a sequential coupling of mechanical, thermal, and wear calculations. Thermal deformation and thermal stress are not solved, and accumulated wear is not fed back to update the vehicle geometry during the simulated run. The brake block supplies braking and thermal boundary conditions; its material loss is outside the present wear calculation.

2.1. Train longitudinal dynamics

For the longitudinal calculation, each locomotive or wagon is represented by a rigid lumped mass, and adjacent vehicles interact through their couplers. The force-balance equation for vehicle i is written as

$$m_i \frac{dv_i}{dt} = -F^{DB} - F_i^B - F_i^W + F_{i-1}^C - F_i^C, \qquad i = 1, ..., n, \tag{2.1}$$

where m_i and v_i represent the mass and longitudinal velocity of vehicle i, respectively, F^{DB} denotes the locomotive dynamic-braking force, F_i^B and F_i^W denote the pneumatic braking force and running resistance acting on vehicle i, and F_i^C represents the force in the coupler joining vehicles i and $i+1$. In this model, $F_0^C = F_n^C = 0$, with n denoting the total number of vehicles.

The locomotive dynamic-braking force is introduced and removed through linear ramps over the prescribed application and release duration t_{DB}.

The pneumatic braking force of the locomotive, F_1^B, is evaluated by the equivalent-conversion relation specified by the National Railway Administration of the People's Republic of China (2018):

$$F_1^B = F_1^H \cdot \varphi_1^H, \tag{2.2}$$

where F_1^H and φ_1^H denote the equivalent total brake-block normal force and its friction coefficient, respectively. Following the National Railway Administration of the People's Republic of China (2018), φ_1^H is evaluated from $\varphi_1^H = 0.382(2v + 150)/(3v + 150)$, where v is the vehicle speed in km/h.

For the wagons behind the locomotive, the pneumatic braking force is evaluated from Eq. (2.3), following the National Railway Administration of the People's Republic of China (2018):

$$F_i^B(t) = \sum_{n_z} K_i(t) \cdot \varphi_i^K(v_i), \qquad i = 2, ..., n, \tag{2.3}$$

where n_z denotes the number of brake blocks fitted to one wagon; the composite brake shoes are used in the C80 wagon, with one brake shoe per wheel; therefore, $n_z = 8$. The brake shoe is made of an asbestos-free organic composite friction material, typically consisting of a thermosetting phenolic-resin binder, reinforcing fibres, friction modifiers, and inorganic fillers. K_i is the block normal force acting on the wheel tread, and φ_i^K denotes the block–tread friction coefficient. The block normal force K_i follows from Eq. (2.4):

$$K_i(t) = \frac{\pi}{4} d_z^2 p_i^B(t) n_b \eta_z \gamma_z \cdot 10^{-6}/n_z, \tag{2.4}$$

where d_z denotes the brake-cylinder inner diameter, $p_i^B(t)$ is the time-varying cylinder pressure, n_b gives the number of cylinders on each wagon, η_z represents the force-transfer efficiency between the cylinder and brake block, and γ_z is the leverage ratio of the wagon rigging. During pneumatic brake application and release, $p_i^B(t)$ of each wagon is calculated with the time-varying model of Nasr and Mohammadi (2010).

Following the National Railway Administration of the People's Republic of China (2018), the block–tread friction coefficient appearing in Eq. (2.3), φ_i^K, is obtained from Eq. (2.5):

$$\varphi_i^K = 0.41 \frac{K_i + 200}{4K_i + 200} \cdot \frac{v_i + 150}{2v_i + 150}. \tag{2.5}$$

The total running resistance is taken as the sum of basic, curve, and gradient resistances, as given in Eq. (2.6):

$$F_i^w = m_i g(w_0 + w_r + w_i), \tag{2.6}$$

where w_0 denotes the basic resistance per unit weight. Following the National Railway Administration of the People's Republic of China (2018), for the locomotive, $w_0 = 1.40 + 0.0038v + 0.0003v^2$, and for a wagon, $w_0 = 0.92 + 0.0048v + 0.000125v^2$. The curve and gradient resistance per unit weight are written as $w_r = 600/R$ and $w_i = i$, respectively, where R denotes the curve radius and i denotes the gradient.

MT–2 couplers are used in the heavy-haul train and are represented by a nonlinear hysteretic loading–unloading relation. The force law and parameter values adopted here are those reported by Liu *et al.* (2022).

Once the braking, resistance, and coupler-force terms have been established for the downhill operation, the Newmark–β scheme is applied to obtain the train velocity and displacement histories.

2.2. Wheel–rail contact analysis

The first wagon is selected for wheel–rail contact evaluation after completion of the longitudinal train simulation. SIMPACK is used here as a multibody dynamics solver for the wagon motion and wheel–rail contact loads. The vehicle comprises a car body and two K6 bogies, with suspension forces represented by force elements. Normal wheel–rail contact follows Hertz theory and the tangential calculation uses FASTSIM. The SIMPACK model of the wagon is shown in Fig. 1. Wheelset braking torque, coupler forces at both wagon ends, and basic resistance are transferred from the train-level calculation. Within SIMPACK, braking torques act on the wheelsets, the two coupler loads act at their respective connection points, and basic resistance is imposed at the wagon centre of gravity. The track is treated as rigid, irregularity is represented by the American Class 5 spectrum, and profile evolution during the simulated run is omitted. The required SIMPACK outputs include the normal contact force F_z, longitudinal and lateral contact forces F_x and F_y, longitudinal and lateral creepages ξ_x and ξ_y, and the lateral wheel contact position y_w. These quantities are passed to the subsequent temperature and tread-wear calculations.

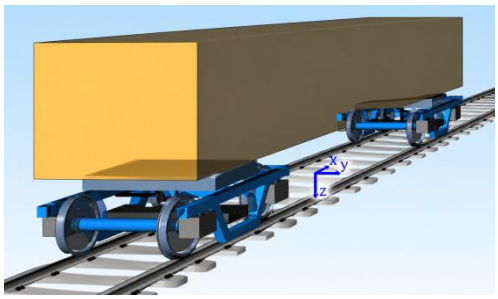


Fig. 1. SIMPACK model of the C80 wagon.

2.3. Wheel temperature rise analysis

On a long downhill descent route, repeated brake applications are used to keep the heavy-haul train within the prescribed speed range. The wheel consequently heats because friction work is produced at both the block–tread and wheel–rail interfaces. The block-induced heat-flux density Φ_{bw} is written as

$$\Phi_{bw} = \frac{F_{bw} v_{bw}}{A_{bw}}, \tag{2.7}$$

where F_{bw} is the tangential block–tread force, v_{bw} denotes wheel circumferential speed, and A_{bw} is the nominal block–tread contact area. At this interface, Φ_{bw} is partitioned into two parts, $\Phi_{bw,b}$ and $\Phi_{bw,w}$, assigned to the block and wheel. The block and wheel temperature rises are

governed by $\Phi_{bw,b}$ and $\Phi_{bw,w}$, respectively. They are calculated from Eq. (2.8) following Magelli (2022):

$$\Phi_{bw,b} = \frac{T_w - T_b}{R_{eb} + R_{ew}} + \frac{\beta_b S_b \Phi_{bw}}{\beta_w S_w + \beta_b S_b}, \qquad \Phi_{bw,w} = \frac{T_b - T_w}{R_{eb} + R_{ew}} + \frac{\beta_w S_w \Phi_{bw}}{\beta_w S_w + \beta_b S_b}, \tag{2.8}$$

where T_w and T_b denote the wheel and block surface temperatures. R_{eb} and R_{ew} are the corresponding areal thermal resistances. β_b and β_w represent the thermal effusivities of the two bodies, and are given by $\beta_b = \sqrt{k_b \rho_b c_b}$, $\beta_w = \sqrt{k_w \rho_w c_w}$. Here k, ρ, and c denote thermal conductivity, density, and specific heat capacity. S_b and S_w denote the effective conduction areas. $S_b = n_b L_b H_b$, where n_b is the number of blocks acting on one wheel and L_b and H_b are block length and width. $S_w = 2\pi R_w H_b$, with R_w denoting the wheel radius.

The frictional heat-flux density Φ_{wr} at the wheel–rail interface is evaluated as

$$\Phi_{wr} = \frac{F_x v_x + F_y v_y}{A_{wr}}, \tag{2.9}$$

where $v_x = \xi_x v$ and $v_y = \xi_y v$ give the longitudinal and lateral relative velocities in the contact, and A_{wr} denotes contact patch area. As for Φ_{bw}, Φ_{wr} is separated into two contributions, $\Phi_{wr,r}$ and $\Phi_{wr,w}$, entering the rail and wheel. Following Qi *et al.* (2026), the partition is obtained from:

$$\Phi_{wr,r} = \frac{T_w - T_r}{R_{er} + R_{ew}} + \frac{\beta_r \sqrt{v}_r \Phi_{wr}}{\beta_r \sqrt{v}_r + \beta_w \sqrt{v}_w}, \qquad \Phi_{wr,w} = \frac{T_r - T_w}{R_{er} + R_{ew}} + \frac{\beta_w \sqrt{v}_w \Phi_{wr}}{\beta_r \sqrt{v}_r + \beta_w \sqrt{v}_w}, \tag{2.10}$$

where T_r denotes rail–surface temperature, R_{er} is the rail areal thermal resistance, and β_r is the rail thermal effusivity, written as $\beta_r = \sqrt{k_r \rho_r c_r}$. v_w and v_r denote the local wheel and rail velocities. Since each wheel encounters a newly exposed rail surface, the rail temperature is set equal to ambient temperature, i.e., $T_r = T_0$.

The layered thermal formulation reported by Qi *et al.* (2026) is used to obtain the wheel temperature history during cyclic braking on the investigated descent. The thermal model assigns a representative temperature to each layer and therefore describes transient heating through the layer discretization. It does not resolve lateral or circumferential hot spots on the wheel tread.

For either body, the heat increment of layer i associated with $\Phi_{i,i+1}$ is evaluated from Eq. (2.11):

$$\Delta Q_i = \left[\Phi_{i-1,i}(t) S_{i-1,i} - \Phi_{i,i+1}(t) S_{i,i+1} - h(t) A_{\mathrm{out},i} (T_i - T_0)\right] \Delta t, \tag{2.11}$$

where ΔQ_i denotes the heat increment of layer i, $S_{i-1,i}$ is the interface area between layers $i-1$ and i, $A_{\mathrm{out},i}$ is the air–exposed area of layer i, T_i is its temperature, and h denotes the convection coefficient. The speed dependence of h follows Zhu *et al.* (2014), with $h = 2.43v + 7.44$. T_0 denotes ambient temperature. The same speed-dependent convection correlation is applied during both brake application and brake release. Thermal radiation is neglected in the present formulation. The convection correlation is adopted from published numerical results. The temperature of every layer is advanced from its calculated heat increment ΔQ_i:

$$T_i(t + \Delta t) = T_i(t) + \frac{\Delta Q_i}{m_i c}, \tag{2.12}$$

where m_i denotes the mass assigned to layer i of the block or wheel.

2.4. Temperature-dependent Archard wear model

The SIMPACK contact solution is based on the Hertz assumption. The semi-axis lengths a_0 and b_0 of the contact patch under ambient temperature are taken directly from the SIMPACK

output. To include wheel heating without modifying the rail properties, the change in the equivalent modulus is approximated by the temperature dependence of the wheel elastic modulus. Accordingly, the semi-axis lengths a_T and b_T are updated with temperature T, in conformity with Eq. (2.13):

$$a_T = a_0 \left(\frac{E_0}{E(T)} \right)^{1/3}, \qquad b_T = b_0 \left(\frac{E_0}{E(T)} \right)^{1/3}, \tag{2.13}$$

where E_0 and $E(T)$ denote the wheel elastic modulus at ambient temperature and at T. The local normal pressure at (x, y) is subsequently obtained from the Hertz pressure distribution. Equation (2.13) is an approximate modulus scaling at fixed normal load and local geometry, based on the Hertzian cube-root dependence (Kalker, 1990).

Once the normal-pressure field has been evaluated, FASTSIM (Kalker, 1982) is used to determine the adhesion and slip regions in the contact patch, as well as the longitudinal and lateral slip velocities v_x and v_y at each point (x, y). The wear-volume increment summed over the contact patch is calculated using the Archard wear model:

$$\Delta V = \sum_{x,y} k_{\text{wear}} \frac{p_T v_s \Delta t}{H(T)} \Delta x \Delta y, \tag{2.14}$$

where ΔV denotes the accumulated contact-patch wear volume, v_s is the resultant local slip speed, $v_s = \sqrt{v_x^2 + v_y^2}$, $H(T)$ is wheel hardness at temperature T, and k_{wear} is the wear coefficient, which depends on the ratio of contact pressure to material hardness and sliding speed (Jendel, 2002), while $\Delta x \Delta y$ is the area represented by node (x, y). Hardness is used as a pressure quantity in Eq. (2.14). The values in Table 3 are expressed in GPa and must be converted consistently with the units used for contact pressure. A hardness test scale cannot be inferred from this pressure unit alone. The tabulated friction coefficient describes wheel–rail contact and is distinct from the block–tread braking coefficients in Eqs. (2.2)–(2.5).

For conversion of wear volume to tread-depth loss, the lateral tread is separated into n_{band} bands. Depth loss in band i follows Eq. (2.15):

$$\Delta z_i = \frac{\Delta V_i}{2\pi R_i \Delta h}, \tag{2.15}$$

where Δz_i and ΔV_i denote depth loss and accumulated volume in band i, R_i is the local wheel radius for that band, and Δh denotes lateral band width. Equation (2.15) follows from dividing the volume accumulated in a lateral band by its circumferential area. The resulting depth is therefore averaged around the wheel circumference. Material removal is evaluated by post-processing; the profile is not updated and wear-induced changes in contact pressure are not included during this run.

Equation (2.16) defines the distance-normalized wear metric. For comparison among operating conditions, the wear rate $\Delta V\prime$ is expressed as accumulated wear volume divided by travelled distance:

$$\Delta V' = \frac{\Delta V}{\Delta s}. \tag{2.16}$$

3. Results and discussion

3.1. Case study configuration

The case study considers wheel wear of a heavy-haul train travelling over a long downhill section of the Datong–Qinhuangdao Railway. The train consists of a two-unit HXD1 electric locomotive and 108 C80 heavy-haul wagons, giving a total train mass of 11,000 t. The investigated

long downhill section is 52 km in length and has an 80 km/h speed limit. The gradient and curve radius data shown in Fig. 2 were obtained from the actual line profile of the investigated section. In the figure, a negative value of the curve radius denotes a right-hand curve in the running direction, whereas a positive value denotes a left-hand curve.

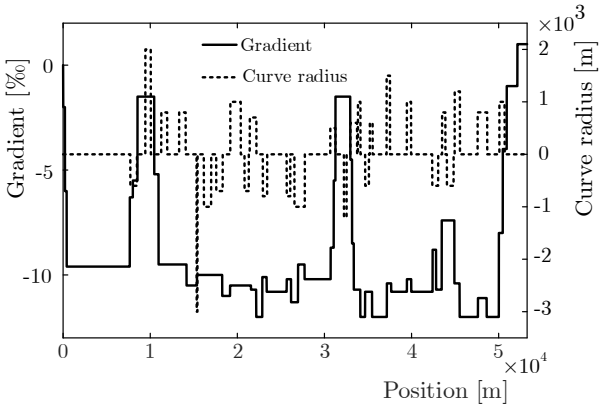


Fig. 2. Gradient profile and curve radii of the downhill section.

The train enters the section at 75 km/h. In the longitudinal simulation, electric and pneumatic braking systems are switched according to the instantaneous speed. At 75 km/h or above, electric braking is applied to the locomotive while pneumatic braking acts on the wagons, causing the train to decelerate. Both braking systems are released when the speed falls to 45 km/h or lower. Table 1 summarizes the parameters used in the longitudinal-dynamics calculation.

Table 1. Parameters used in the longitudinal dynamic simulation of the heavy-haul train.

	Parameter	Value	Parameter	Value	Parameter	Value
Locomotive	Mass	2×10^5 kg	Length	35.2 m	F^D	461 kN
	t_{DB}	5 s	F_1^H	100 kN		
Wagon	Mass	10^5 kg	Length	12m̀		
Air braking model	d_z	305 mm	n_b	1	η_z	0.9
	γ_z	7.3	$P_{\max}$	90 kPa		

The C80 wagon model described in Section 2.2 is adopted for the multibody-dynamics calculation. Each K6 three-piece bogie contains wheelsets, side frames, and a bolster. Track flexibility is not considered. The LM wheel and CHN60 rail profiles commonly used in China are selected.

Train speed and the pneumatic braking force on each wheel are supplied by the longitudinal model, while the C80 SIMPACK simulation provides longitudinal and lateral creep velocities and forces. These outputs are used to evaluate the instantaneous frictional heat input. For the transient thermal calculation, both the brake block and the wheel are separated into ten layers. Layer mass, interlayer heat-transfer area, and surface area exposed to air are obtained from the corresponding finite-element models. The formulation in Section 2.3 is then used to calculate block and wheel temperatures produced jointly by tread braking and wheel–rail creepage. The adopted thermal parameters are listed in Table 2.

The temperature-dependent parameters adopted for the wear calculation are listed in Table 3, with the source studies identified as Talamini *et al.* (2005) and Chen and Lee (2009). Within this adopted dataset, Young's modulus, hardness, and the wheel–rail friction coefficient decrease as temperature increases. Hardness values were estimated on the Brinell scale from temperature-dependent tensile strength, using the room-temperature hardness as a reference, and converted to GPa for the Archard wear calculation. The modulus correction enlarges the Hertz contact ellipse

Table 2. Main parameters used in the wheel temperature analysis.

Category	Quantity	Wheel	Brake block	Rail
Geometry	Wheel radius [m]	0.420	–	–
	Block length [m]	–	0.32	–
	Block width [m]	–	0.08	–
Interface	Nominal block–wheel area [m^2]	0.0256	Shared interface	–
Material	Conductivity [W/(m K)]	50	2.14	50
	Density [kg/m^3]	7818	1787	7818
	Specific heat [J/(kg K)]	487	986	487
Thermal boundary	Areal thermal resistance [m^2 K/W]	6.65×10^{-6}	1.40×10^{-3}	1.31×10^{-5}
	Ambient temperature [°C]	25	25	25

Table 3. Temperature-dependent wheel material parameters.

Temperature [°]	Young's modulus [GPa]	Poisson ratio	Friction coefficient	Hardness [GPa]
24	213	0.300	0.334	3.209
230	201	0.307	0.263	3.141
358	193	0.314	0.225	3.120
452	172	0.320	0.197	3.081

at a fixed normal load and reduces its maximum pressure. The friction trend is an assumed input for the present calculation, rather than a universal temperature law for wheel–rail or brake-block materials.

3.2. Analysis results

The longitudinal response of the train under cyclic braking is evaluated first. The leading wagon behind the locomotive is then used for the wheel–rail dynamics and wear calculations. Figure 3 presents its speed along the downhill section as predicted by the longitudinal model.

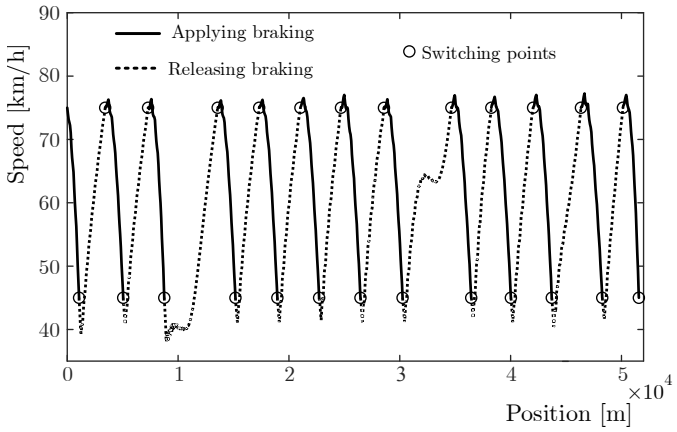


Fig. 3. Speed curve of the wagon running on the long downhill section.

Cyclic braking limits the train speed, and the corresponding wheelset braking torque is plotted in Fig. 4a. Coupler loads at the front and rear of the wagon also contribute to its longitudinal response and are obtained from the longitudinal dynamics simulation. Figure 4b gives the front coupler force of the first wagon; negative and positive values denote compression and tension, respectively. During brake application, the high locomotive electric braking force, whose maximum

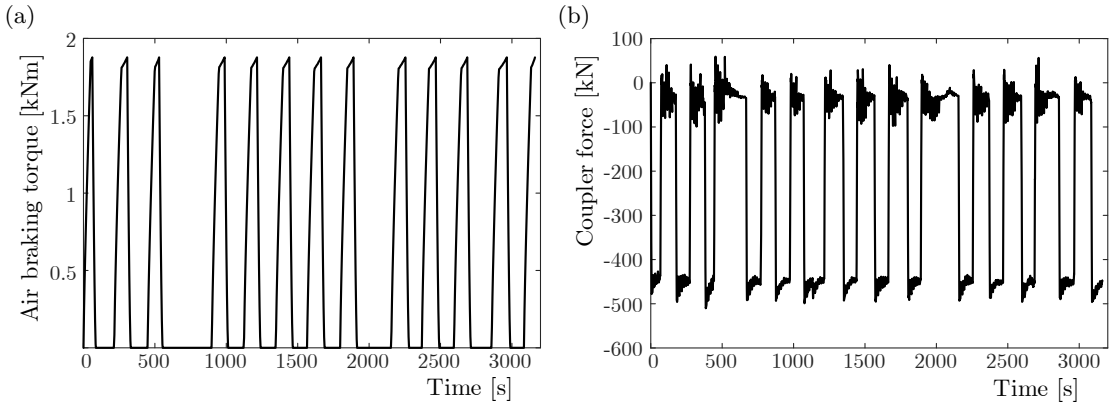


Fig. 4. Train longitudinal dynamics: (a) wheelset braking torque; (b) front coupler force.

is 461 kN, places the coupler in compression. The largest compressive force in the brake application phase is about 500 kN. In the brake release phase, the coupler force oscillates close to 0 kN.

The measured gradient, curve radius, superelevation, and transition geometry are implemented in SIMPACK. Coupler force histories, wheelset braking torques, and the wagon basic resistance are then imposed on the vehicle model to reproduce the downhill operation. Figure 5 compares the SIMPACK speed with that calculated by the longitudinal model. The small difference provides an internal consistency check on the transferred motion and loading histories; it does not independently validate the contact, temperature, or wear predictions.

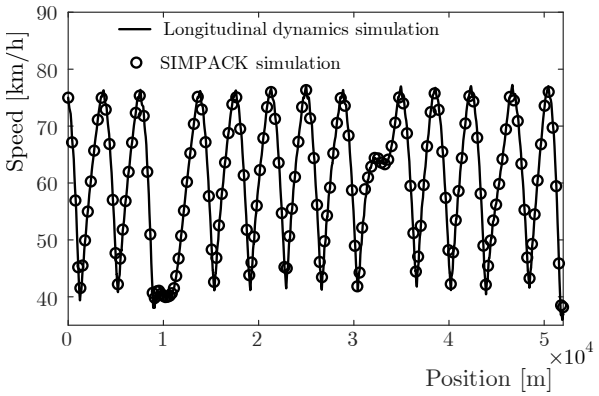


Fig. 5. Comparison of speed curves obtained from the longitudinal dynamic simulation and the SIMPACK simulation.

The pneumatic braking force and train speed from the longitudinal simulation, together with creep velocities and forces from SIMPACK, drive the transient thermal calculation. Figure 6 plots the modelled representative wheel and block surface temperatures against distance along the route. "Position [m]" denotes distance from the beginning of the investigated section, not depth below a friction surface. The temporal peaks are 339.8 °C for the wheel and 282.8 °C for the block; they should not be interpreted as maximum local temperatures in resolved three-dimensional fields. The wheel and block temperatures reflect their different heat inputs, thermal properties, effective areas, and heat-transfer paths. For context, Li *et al.* (2019) reported a peak wheel temperature of approximately 325 °C in a published braking case with an initial speed of 75 km/h. Relative to that reported value, the difference is approximately 4.55 %. This comparison is only a plausibility check on temperature magnitude, because a fully matched benchmark and a new full-scale braking experiment are not established here.

The SIMPACK outputs used in the wear calculation are the normal and tangential contact forces, tangential and spin creepages, and the lateral contact position. After temperature-

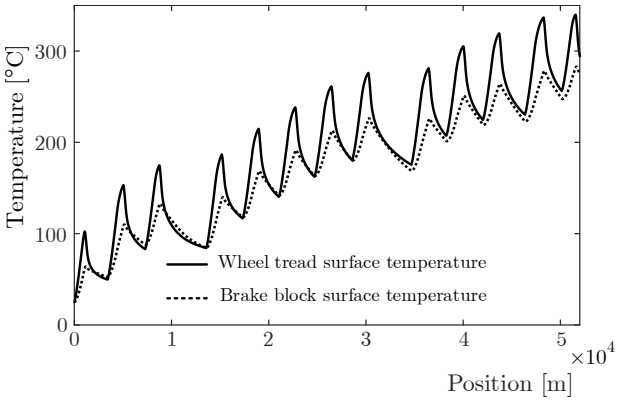


Fig. 6. Surface temperature evolution of the wheel and brake block under cyclic braking.

dependent wheel properties are introduced, the Hertz model provides the contact semi-axes and normal-pressure distribution. FASTSIM then resolves adhesion and slip and gives the local slip velocity at each point (x, y). The temperature-dependent Archard model is used to obtain the wear volume, ΔV. For lateral mapping, the tread region extends from -30 mm to $+30$ mm relative to the nominal rolling circle and is divided into 600 uniformly spaced wear bands, each 0.1 mm wide. Each contact-patch contribution is accumulated in the corresponding band, and band wear depth is calculated from Eq. (2.15). Figure 7 presents the resulting wear-depth distributions for the front-bogie wheels after the 52 km downhill run under cyclic braking.

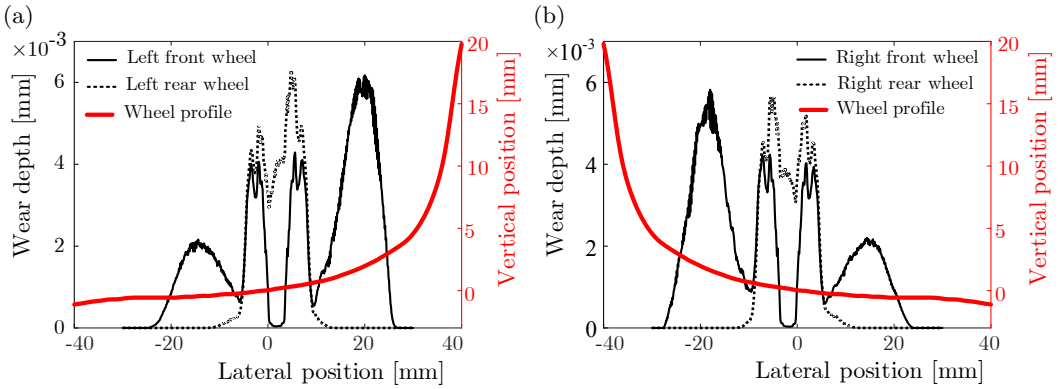


Fig. 7. Circumferentially averaged lateral wheel tread wear depth accumulated after one 52 km downhill run for the leading wagon's front bogie: (a) left wheels; (b) right wheels.

As shown in Fig. 7, the maximum wear depths of the front and rear wheels are both approximately 0.006 mm. However, the total wear volume of the front wheel is larger than that of the rear wheel, and the wear distributions of the front and rear wheels are markedly different. For the left front wheel, the wear region extends from approximately -25 mm to 27 mm, which is wider than that of the rear wheel. The maximum wear depth occurs at approximately 20 mm, close to the flange side. In the central tread region from -2 mm to 4 mm, the wear depth is very small. After repeated operation on long downhill lines, this uneven wear may promote a local protrusion on the wheel tread. On the left side, the rear wheel exhibits a narrower wear region, ranging from approximately -10 mm to 10 mm, with the maximum wear depth occurring near -5 mm. The accumulated wear in this region may contribute to hollow tread wear. The wear characteristics of the rear bogie are generally consistent with those of the front bogie.

The left front wheel of the leading bogie is used to compare the effects of tread braking and track curvature on the wheel tread wear rate. The data are separated by braking state, by tread-temperature ranges below 200 °C, 200 °C to 300 °C, and above 300 °C, and by straight

or curved track. For each group, accumulated wear volume is divided by the associated travel distance according to Eq. (2.16). The resulting mean wear rates are presented in Fig. 8.

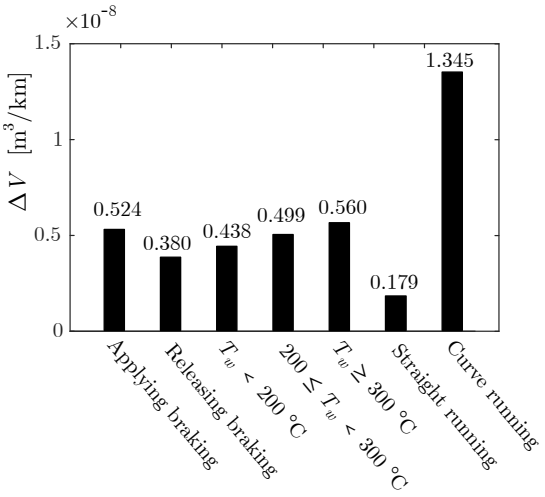


Fig. 8. Mean wheel wear rate under different operating conditions.

Figure 8 shows a higher route-grouped mean wear rate during brake application than during release, with a ratio of 1.380. Braking changes wheel–rail creepage and thereby affects wear. Under the adopted temperature-dependent inputs, the modulus and hardness decrease and the wheel–rail friction coefficient also decreases. Their combined effects change contact area, pressure, and local slip; they cannot be separated by temperature grouping alone. The mean wear rates at 200 °C to 300 °C and above 300 °C are 1.139 and 1.279 times that below 200 °C, respectively. The curved-track mean is 7.514 times the straight-track mean. This is the largest of the reported route-grouped ratios, but the groups also differ in speed, braking history, the contact state, and distance exposure. These ratios describe the investigated route and do not independently establish causal sensitivities or a universal ranking of the three factors.

The braking effect is examined in greater detail by comparing mean wear rates on curves of different radii with those on straight track, as plotted in Fig. 9.

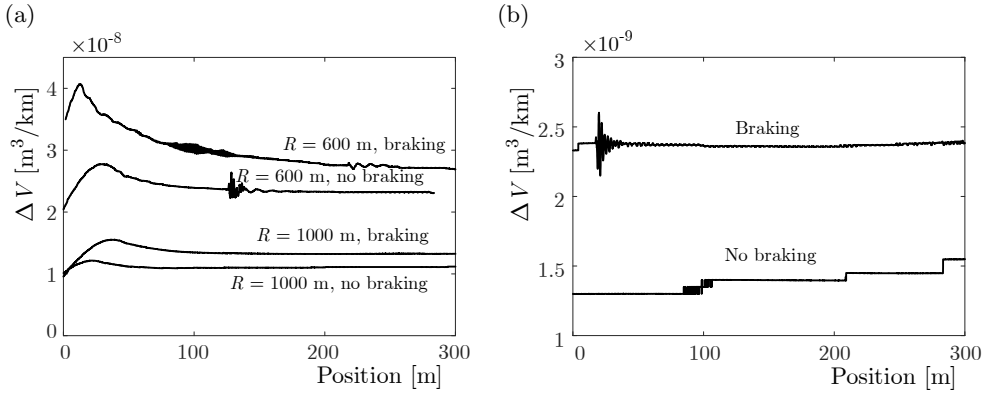


Fig. 9. Effects of tread braking on wheel wear rate: (a) wear rate on curved track; (b) wear rate on straight track.

Figure 9 shows that during brake application, block–wheel friction increases wheel–rail creepage and aggravates the tread wear rate. Figure 9a shows that this increase becomes larger as the curve radius decreases. Braking also raises the straight-track wear rate, as seen in Fig. 9b, where the mean value is 1.709 times that obtained during release. Nevertheless, the baseline wear on tangent track is small, and its braking value remains well below the corresponding values on curves.

Block–wheel friction affects wear through both the mechanical braking action and the associated wheel heating. Temperature-induced changes in material properties and wheel–rail contact conditions can therefore further increase material loss. To compare their combined effects, wear on an 800 m radius curve is evaluated for braking and release at low and high temperature. Figure 10 presents the comparison.

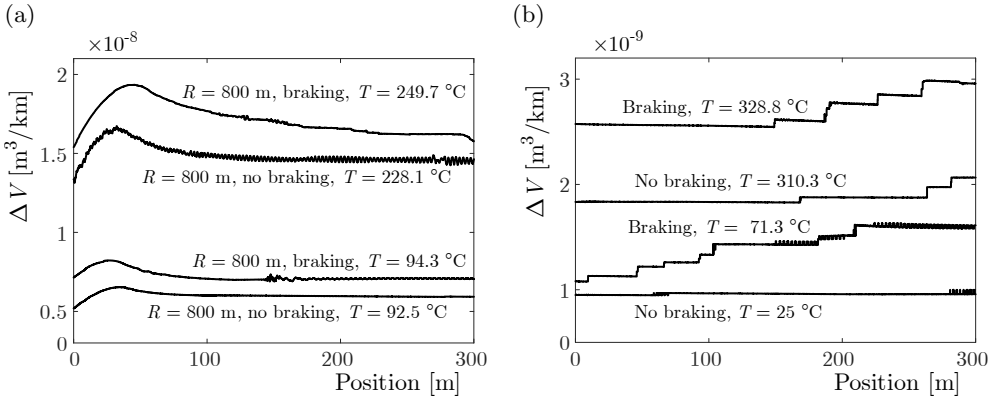


Fig. 10. Effects of tread braking and wheel temperature rise on wheel wear rate: (a) wheel running on curved track; (b) wheel running on straight track.

For the curved track cases in Fig. 10a, applying the brake increases wear, and the increase is greater at the higher temperature. Figure 10b gives the corresponding straight-track results. Braking and tread heating again raise the wear rate, although all straight-track values remain much lower than those on the curve. These comparisons are consistent with higher wear under combined braking and elevated-temperature conditions in the adopted model. Isolating the contribution of hardness or friction requires recalculation with otherwise identical mechanical inputs.

4. Conclusions

A sequential calculation framework combining train longitudinal dynamics, a three-dimensional vehicle multibody model, reduced-order wheel–block thermal analysis, and temperature-dependent Archard wear were applied to a 52 km downhill route. The framework links cyclic braking and route geometry with contact loading, nominal frictional heating, and wheel–rail wear post-processing. The predicted representative wheel-tread temperature reaches 339.8 °C, and the accumulated circumferentially averaged wear depth varies across the tread after one run. Route-grouped mean wear rates are higher during braking, in higher-temperature groups, and on curved track. The curved-to-straight-track ratio is the largest observed comparison; these grouped results should not be interpreted as independent causal sensitivities. Curved downhill sections are therefore a priority for further wheel-wear assessment. The calculation does not resolve three-dimensional thermal fields, thermal stresses, brake-block material loss, or feedback from profile evolution. The predicted temperatures and wear magnitudes depend on the adopted thermal boundary conditions and temperature-dependent material and contact parameters. Direct validation of the absolute wear predictions remains limited. Further validation against temperature and wear measurements under comparable cyclic braking conditions is therefore needed before applying the framework to quantitative maintenance planning.

Acknowledgments

The work was supported by the National Natural Science Foundation of China under grant no. 12262017.

References

1. Akama, M. (2025). Rolling contact fatigue and wear of rails and wheels: A comprehensive review. *Machines*, *13*(10), Article 970. https://doi.org/10.3390/machines13100970
2. Chen, Q., Xiao, Q., Chen, S., Ran, X., Hu, X., Jin, Y., Xu, B., & Wang, K. (2026). Research on wheel damage of heavy-haul locomotive subjected to longitudinal coupler forces: Formation mechanism and control measures from macro insight. *Engineering Failure Analysis*, *186*(Part A), Article 110482. https://doi.org/10.1016/j.engfailanal.2025.110482
3. Chen, S., Wu, L., Zhang, H., Wen, Z., & Wang, H. (2017). Influence of temperature rising of tread braking on wheel wear for heavy haul freight car (in Chinese). *Journal of Mechanical Engineering*, *53*(2), 92–98. https://doi.org/10.3901/JME.2017.02.092
4. Chen, Y.-C., & Lee, S.-Y. (2009). Elastic-plastic wheel-rail thermal contact on corrugated rails during wheel braking. *Journal of Tribology*, *131*(1), Article 011401. https://doi.org/10.1115/1.2991163
5. Doan Van, D., Nguyen Huu, P., Vo Dinh, H., & Tran Cong, T. (2026). A multibody dynamics-based investigation of wheel-rail wear and rolling contact fatigue for high-speed railway applications in Vietnam. *Railway Sciences*, *5*(3), 411–435. https://doi.org/10.1108/RS-03-2026-0021
6. Handa, K., Ikeuchi, K., & Morimoto, F. (2020). Temperature-dependent wear of tread-braked railway wheels. *Wear*, 452–453, Article 203265. https://doi.org/10.1016/j.wear.2020.203265
7. Jendel, T. (2002). Prediction of wheel profile wear—comparisons with field measurements. *Wear*, *253*(1–2), 89–99. https://doi.org/10.1016/S0043-1648(02)00087-X
8. Kalker, J.J. (1982). A fast algorithm for the simplified theory of rolling contact. *Vehicle System Dynamics*, *11*(1), 1–13. https://doi.org/10.1080/00423118208968684
9. Kalker, J.J. (1990). Three-dimensional elastic bodies in rolling contact. Springer Dordrecht. https://doi.org/10.1007/978-94-015-7889-9
10. Li, L., Cai, Y., & Guo, G. (2019). Coupling effect of wheel-rail rolling contact and braking thermal load on crack initiation life of heavy haul wheel tread (in Chinese). *China Railway Science*, *40*(3), 89–96.
11. Liu, S., He, Q., Fu, W., & Feng, Q. (2025). A two-step data-driven method for predicting the wear of train wheel treads using GA-BPNN and LSTM algorithms. *International Journal of Rail Transportation*, *13*(1), 85–102. https://doi.org/10.1080/23248378.2024.2324092
12. Liu, W., Su, S., Tang, T., & Cao, Y. (2022). Study on longitudinal dynamics of heavy haul trains running on long and steep downhills. *Vehicle System Dynamics*, *60*(12), 4079–4097. https://doi.org/10.1080/00423114.2021.1998559
13. Liu, X., Zhang, S., Fang, W., Wang, W., & Cong, T. (2026). The failure analysis of circumferential cracks on the wheel tread in railway freight train. *Engineering Failure Analysis*, *184*, Article 110298. https://doi.org/10.1016/j.engfailanal.2025.110298
14. Magelli, M. (2022). Development of a 2D finite element model for the investigation of the tread braked railway wheels thermo-mechanical behaviour. *IOP Conference Series: Materials Science and Engineering*, *1214*(1), Article 012041. https://doi.org/10.1088/1757-899X/1214/1/012041
15. Magelli, M., & Zampieri, N. (2024). Calculation of wear of railway wheels with multibody codes: Benchmarking of the modelling choices. *Machines*, *12*(9), Article 644. https://doi.org/10.3390/machines12090644
16. Miao, G., Luo, R., & Shi, H. (2024). Wheel wear prediction for high-speed trains by considering wheel-rail elastic deformation. *Proceedings of the Institution of Mechanical Engineers, Part F: Journal of Rail and Rapid Transit*, *238*(8), 921–930. https://doi.org/10.1177/09544097241239089
17. Nasr, A., & Mohammadi, S. (2010). The effects of train brake delay time on in-train forces. *Proceedings of the Institution of Mechanical Engineers, Part F: Journal of Rail and Rapid Transit*, *224*(6), 523–534. https://doi.org/10.1243/09544097JRRT306
18. National Railway Administration of the People's Republic of China. (2018). *Railway train traction calculation – Part 1: Trains with locomotives* (TB/T 1407.1–2018) (in Chinese). China Railway Publishing House.

19. Qi, Y., Jing, H., Luo, S., Wang, J., Zheng, Y., & Zhao, G. (2026). Thermal analysis of heavy-haul freight wagon wheel-block under operating conditions. *Tribology Transactions*, *69*(2), 229–240. https://doi.org/10.1080/10402004.2025.2584252

20. Talamini, B., Gordon, J., & Perlman, A.B. (2005). Investigation of the effects of sliding on wheel tread damage. *Proceedings of the ASME 2005 International Mechanical Engineering Congress and Exposition, USA*, *IMECE2005-82826*, 119–125. https://doi.org/10.1115/IMECE2005-82826

21. Wang, B., Wu, Q., Luo, S., Spiryagin, M., Ma, W., Ding, H., & Yang, Z. (2024). Wheel tread temperature assessment and its impact on rolling contact fatigue under long-term braking conditions. *Tribology International*, *200*, Article 110162. https://doi.org/10.1016/j.triboint.2024.110162

22. Wen, B., Tao, G., & Wen, Z. (2025). Prediction of locomotive wheel wear evolution considering thermo-mechanical coupling: Wear model and validation. *Wear*, *571*, Article 205805. https://doi.org/10.1016/j.wear.2025.205805

23. Wu, Q., Bernal, E., Spiryagin, M., Krishna, V., Ding, H., Stichel, S., & Cole, C. (2024). Heavy haul rail/wheel wear and RCF assessments using 3D train models and a new wear map. *Wear*, *538–539*, Article 205226. https://doi.org/10.1016/j.wear.2023.205226

24. Ye, Y., Huang, C., Zeng, J., Wang, S., Liu, C., & Li, F. (2023). Predicting railway wheel wear by calibrating existing wear models: Principle and application. *Reliability Engineering & System Safety*, *238*, Article 109462. https://doi.org/10.1016/j.ress.2023.109462

25. Zhang, S., Liu, Q., Spiryagin, M., Wu, Q., Ding, H., Wen, Z., & Wang, W. (2023). Gaps, challenges and possible solution for prediction of wheel–rail rolling contact fatigue crack initiation. *Railway Engineering Science*, *31*(3), 207–232. https://doi.org/10.1007/s40534-023-00302-8

26. Zhu, L., Wang, L., & Shi, W. (2014). Calculation of convective heat transfer coefficient for locomotive wheels (in Chinese). *Computer Aided Engineering*, *23*(1), 21–24.

27. Zou, R., Yang, L., Wu, Q., Cole, C., & Spiryagin, M. (2026). Common cause and dynamic influence analyses for railway air brake hose failures. *Engineering Failure Analysis*, *194*, Article 110968. https://doi.org/10.1016/j.engfailanal.2026.110968

Manuscript received July 28, 2026; accepted for publication October 12, 2026; published online November 27, 2026.